

Suzaku Observation of the Intermediate Polar V1223 Sagittarii

Takayuki HAYASHI^{1,2}, Manabu ISHIDA^{1,2}, Yukikatsu TERADA³, Aya BAMBA^{4,1,5},
and Takeshi SHIONOME^{1,2}

¹ *Institute of Space and Astronautical Science(ISAS) /JAXA, 3-1-1 Yoshinodai, Chuo-ku, Sagamihara,
Kanagawa 252-5210*

thayashi@astro.isas.jaxa.jp

² *Department of Physics, Tokyo Metropolitan University, 1-1 Minami-Osawa, Hachioji, Tokyo, 192-0397*

³ *Department of Physics, Science, Saitama University, Sakura, Saitama 338-8570*

⁴ *School of Cosmic Physics, Dublin Institute for Advanced Studies, 31 Fitzwilliam Place, Dublin 2, Ireland*

⁵ *Department of Physics and Mathematics, College of Science and Engineering, Aoyama Gakuin University
5-10-1 Fuchinobe, Chuo-ku, Sagamihara, Kanagawa, 252-5258, Japan*

(Received ; accepted)

Abstract

We report on the Suzaku observation of the intermediate polar V1223 Sagittarii. Using a multi-temperature plasma emission model with its reflection from a cold matter, we obtained the shock temperature to be $37.9_{-4.6}^{+5.1}$ keV. This constrains the mass and the radius of the white dwarf (WD) in the ranges $0.82_{-0.06}^{+0.05} M_{\odot}$ and $(6.9 \pm 0.4) \times 10^8$ cm, respectively, with the aid of a WD mass-radius relation. The solid angle of the reflector viewed from the post-shock plasma was measured to be $\Omega/2\pi = 0.91 \pm 0.26$. A fluorescent iron $K\alpha$ emission line is detected, whose central energy is discovered to be modulated with the WD rotation for the first time in magnetic-CVs. Detailed spectral analysis indicates that the line comprises of a stable 6.4 keV component and a red-shifted component, the latter of which appears only around the rotational intensity-minimum phase. The equivalent width (EW) of the former stable component ~ 80 eV together with the measured Ω indicates the major reflector is the WD surface, and the shock height is not more than 7% of the WD radius. Comparing this limitation to the height predicted by the Aizu model (1973), we estimated the fractional area onto which the accretion occurs to be $< 7 \times 10^{-3}$ of the WD radius, which is the most severe constraint in non-eclipsing IPs. The red-shifted iron line component, on the other hand, can be interpreted as emanating from the pre-shock accretion flow via fluorescence. Its EW (28_{-13}^{+44} eV) and the central energy ($6.30_{-0.05}^{+0.07}$ keV) at the intensity-minimum phase are consistent with this interpretation.

Key words: accretion, accretion columns— plasma — stars: intermediate polar (IP) — X-rays: individual (V1223 Sagittarii)

1. Introduction

Cataclysmic variables (CVs) are binaries composed of a white dwarf (WD) and a main sequence star or a red giant that fills its Roche lobe. Of them, a group of systems harbouring a magnetized WD ($B < 10$ MG) whose rotation is not synchronized with the secondary rotation is referred to as an intermediate polar (IP). In the IPs, matter spilt over the Roche lobe of the secondary star is funneled into the accretion columns by the strong magnetic field within the Alfvén radius, and falls toward the WD surface nearly at the free fall speed. Since the accreting matter becomes highly supersonic as it descends the column, a strong standing shock is formed close to the WD surface, and the matter is heated up to a temperature of

$$kT_s = \frac{3}{8} \frac{GM}{R} \mu m_H = 16 \left(\frac{M}{0.5 M_\odot} \right) \left(\frac{R}{10^9 \text{cm}} \right)^{-1} \text{ [keV]} \quad (1)$$

(Hōshi 1973; Aizu 1973). The high temperature plasma thus formed is cooled via optically thin thermal plasma emission, and finally settles onto the WD surface. Since the accretion is inhomogeneous, the X-ray intensity from the IPs are modulated at the WD rotational period. The modulation is considered to be due mainly to photoelectric absorption by the pre-shock accreting matter. As a result, the modulation depth increases with decreasing X-ray energy, and the pulse-intensity-minimum occurs when one of the accretion columns becomes closest to the observer's line of sight (Rosen et al. 1988).

Since the maximum temperature of the plasma is proportional to the gravitational potential of the WD as shown in Eq. (1), the WD mass can be estimated by evaluating the maximum temperature with an X-ray continuum measurement. Although this approach has been tried so far in a number of works (Beuermann et al. 2004; Revnivtsev et al. 2004; Suleimanov et al. 2005; Evans & Hellier 2007; Brunschweiler et al. 2009; Yuasa et al. 2010), it is not so straightforward. First, the temperature distribution described above should be taken into account in the emission model. Second, the observed X-ray emission is contaminated by the plasma emission reflected off from the WD surface as well as the pre-shock accreting matter (Ezuka & Ishida 1999), whose spectra is significantly different from the direct spectrum. Third, the line-of-sight hydrogen column density also has a distribution with a maximum column of $N_H \simeq 10^{23.5} \text{ cm}^{-2}$ (Ezuka & Ishida 1999). All these effects should be carefully considered in evaluating the mass from the X-ray continuum emission.

On the other hand, the intensity of the reflected continuum is useful in evaluating the geometry of the hot plasma. In addition to the continuum, an iron emission line at 6.4 keV emanates from the same reflector via fluorescence. Its equivalent width (EW) is useful for evaluating the solid angle of the reflector viewed from the plasma (Makishima 1996; George & Fabian 1991). Since part of the 6.4 keV line is emitted from the pre-shock accreting matter, its central energy modulation at the WD rotational period may be detected from some IPs.

In order to measure the WD mass more accurately than ever and to elucidate the geometry of the accretion column by means of a better evaluation of the intensities of the reflected continuum and the 6.4 keV iron line, we have carried out the observation of the typical IP V1223 Sagittarii (4U1849-

Table 1. Suzaku observation log of V1223 Sagittarii.

Sequence #	Observation date (UT)	Pointing	Detector*	Mode	Exposure [†] (ksec)	Intensity [‡] (count s ⁻¹) [§]
402002010	2007 Apr 13 11:31-14 22:36	HXD nom.	XIS	Normal	60 sec	10.54 ^{+0.03} _{-0.02}
			HXD-PIN	Normal	46 sec	0.57±0.01

* XIS: XIS0,1,3 are combined.

[†]Exposure time after data screening.

[‡]Intensity in the 0.1-11.5 keV for the XIS and in the 12-50 keV band for the HXD-PIN with 1 σ error.

[§] XIS0, 1, 3 are combined.

31) with Suzaku (Mitsuda et al. 2007). High spectral resolution of the X-ray Imaging Spectrometer (XIS) as well as high sensitivity of the Hard X-ray Detector (HXD) above 10 keV are ideal combination to carry out this investigation. V1223 Sgr locates at $\ell = 4^{\circ}57'28''.9$, $b = -14^{\circ}21'16''.8$ which was identified by HEAO 1 (Steiner et al. 1981). V1223 Sgr shows a pulsation at the spin period of the WD of $P_{\text{spin}} = 745.6$ s (Osborne et al. 1985), and an intensity modulation at an orbital period of $P_{\text{orb}} = 3.37$ hr (Jablonski & Steiner 1987). Additional intensity modulation at the beat period between them ($P_{\text{beat}} = 794.4$ s) is also detected (Steiner et al. 1981). The distance and the orbital inclination are known to be $D = 527$ pc and $i = 24^{\circ}$, respectively (Beuermann et al. 2004). The mass of the WD evaluated from the previous works, on the other hand, distributes in a wide range of 0.71–1.046 M_{\odot} (see table 4).

This paper is organized as follows. In § 2, we introduce the instruments onboard Suzaku and show the observation log and the procedure of the data reduction. In § 3, details of our timing and spectral analysis are presented. The high spectral resolution and the wide-band coverage enable us to determine the X-ray spectral parameters with unprecedented accuracy. In § 4, we discuss the mass of the WD and the geometry of the post-shock plasma in V1223 Sgr, and the spin modulation of the fluorescent iron $K\alpha$ line. In § 5, we summarize our results and discussions.

2. Observation and Data Reduction

2.1. Observation

The Suzaku observation of V1223 Sgr (Seq.#402002010) was carried out from 2007 April 13 11:31 (UT) to April 14th 22:36 (UT). The observation log is summarized in table 1. Suzaku is equipped with four modules of the XIS (Koyama et al. 2007), which are designed as XIS0, XIS1, XIS2, and XIS3. Of them, XIS1 adopts a back-illuminated (BI) CCD, while the other three employ front-illuminated (FI) CCDs. They cover energy ranges of 0.2–10 keV and 0.4–10 keV, respectively. The energy resolution of them is ~ 150 eV (FI) and ~ 160 eV (BI) in FWHM at 6 keV at the time of

this observation.¹ The energy calibration accuracy at the Mn-K α line (5.895 keV) is $\lesssim 5$ eV.^{2, 3} One of the modules XIS2 has been unusable since 2006 November, and hence we use the other three XIS modules in this paper.

Each XIS module is located in the focal plane of an X-ray telescope (XRT: Serlemitsos et al. 2007). The XRT adopts Wolter-I type grazing-incident reflective optics consisting of tightly nested, thin-foil conical mirror shells. The angular resolution ranges from 1'8 to 2'3 in half-power diameter. The effective area is 440 cm² at 1.5 keV and 250 cm² at 8 keV per XRT module.

The energy range above 10 keV is covered with the HXD, which is a non-imaging, collimated detector (Takahashi et al. 2007; Kokubun et al. 2007). It is composed of the two detectors. One is the PIN detector which adopts 2 mm-thick silicon PIN diodes, and is sensitive to an X-ray energy in 10–70 keV. the other is a GSO/BGO phoswich counter which is sensitive in the 40–600 keV band. The energy resolution is 3.0 keV (FWHM) for the PIN detector, and $7.6\sqrt{E}\%$ (FWHM) for the GSO detector, where E is energy in MeV. Since we have detected no significant flux with the GSO, we only use the PIN data in this paper.

Throughout the observation of V1223 Sgr, the XIS was operated in the normal 5 \times 5 and 3 \times 3 editing modes during the data rate SH/H and M/L, respectively. Spaced-row Charge Injection (SCI) (Nakajima et al. 2008) is applied while no window/burst options is used. The HXD PIN was operated with a bias voltage of 500 V for 8 out of 64 modules and 400 V for the others to suppress the rapid increase of noise events, possibly caused by in-orbit radiation damage.

The observation was performed at the HXD nominal position in order to collect more photons over 10 keV where the reflection continuum stands out.

2.2. Data Reduction

We used the datasets produced by the Suzaku pipe-line processing version 2.0.6.13 with the calibration files of hxd20070710, xis20070731, and xrt20070622 for the HXD, XIS, XRT, respectively. We analyzed the data with the analysis software package HEASOFT version 6.3.1 and XSPEC version 12.5.1 (Arnaud 1996). For the XIS analysis, we employed photons with the ASCA grades of 0, 2, 3, 4, 6 events. We discarded the data while the satellite telemetry was saturated and the telemetry data rate was L in which the telemetry usually saturates. Furthermore we excluded the data taken while the earth elevation angle is less than 5 $^\circ$ (ELV<5), the day-earth elevation angle is less than 20 $^\circ$ (DYE_ELV<20), and the spacecraft passes in the South Atlantic Anomaly. As a result, the total exposure time of the XIS is about 60 ks. We employed a circular region with a radius of 250 pixels (4'34) centered on the V1223 Sgr image as the integration region of the source photons, which includes more than 96% flux from the source. The background photons are collected from an annulus between radii of 250 pixels and 500 pixels centered on V1223 Sgr. The source and the background

¹ http://www.astro.isas.jaxa.jp/suzaku/process/caveats/caveats_xrtxis06.html

² <http://www.astro.isas.jaxa.jp/suzaku/doc/suzakumemo/suzakumemo-2007-06.pdf>

³ <http://www.astro.isas.jaxa.jp/suzaku/analysis/xis/sci/>

regions are drawn on the observed X-ray image in Fig. 1. The background-subtracted mean intensity

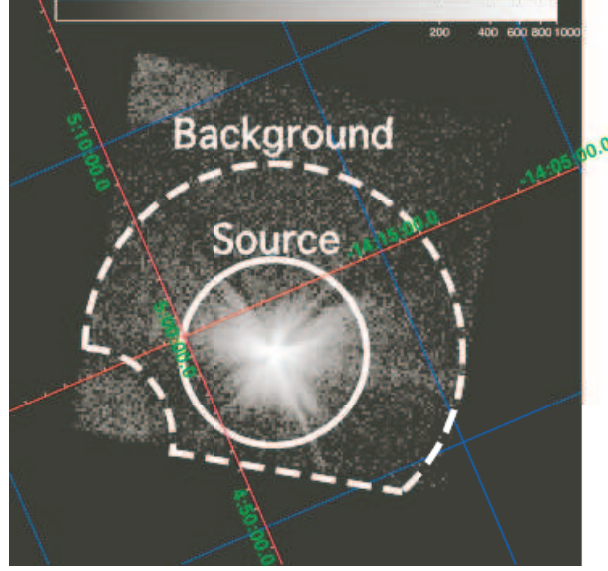


Fig. 1. The image of the V1223 Sgr with XIS0 in the galactic coordinate, and the integration regions of source and background photons. The gray scale represents the X-ray surface brightness in a logarithmic scale. The source region is a circle with a radius of $4'34''$ centered on the source, while the background region is an annulus with an outer radius of $9'$ out of the source integration region. The bright regions at the upper and lower left corners are irradiated with the onboard ^{55}Mn sources.

of the XIS is $10.54^{+0.03}_{-0.02}$ counts sec^{-1} in 0.1-11.5 keV with the three XIS modules.

We employed nearly the same data selection criteria to the HXD as to the XIS. We, however, did not apply the day-earth elevation criterion ($\text{DYE_ELV} < 20$), but instead, we discarded the data while the cutoff rigidity is less than 6 GeVc^{-1} . As a result, we obtained about 46 ksec exposure time for the HXD PIN.

We adopted the “tuned” non-X-ray background (NXB) event file provided by the HXD team, using `METHOD = "LCFITDT (bgd_d)"` and version of `METHODV = "2.0ver0804"` (Fukazawa et al. 2009), and synchronized GTIs (good time intervals) of this with that of the source event file. Eventually, averaged intensity in energy band of 12-50 keV after the NXB subtraction is $0.57 \pm 0.01 \text{ c s}^{-1}$. In addition to this, for spectrum analysis, we considered cosmic X-ray background (CXB). Following results based on HEAO-1 observation (Boldt 1987), we assumed the CXB spectrum of

$$f_{\text{CXB}(E)} = 9.0^{-9} \times \left(\frac{E}{3\text{keV}} \right)^{-0.29} \times \exp \left(-\frac{E}{40\text{keV}} \right) \text{ erg cm}^{-2}\text{s}^{-1}\text{str}^{-1}\text{keV}^{-1}. \quad (2)$$

According to this equation, the intensity of the CXB is found to be equal to $\sim 5 \%$ of the NXB in the 12–50 keV band. We created a CXB spectrum file from Eq. (2) by the `fakeit` command in XSPEC using HXD PIN flat sky response file `ae_hxd_pinflat3_20081029.rsp`, assuming that the uniform emission is from a sky region of $2^\circ \times 2^\circ$.

⁴ http://heasarc.gsfc.nasa.gov/docs/suzaku/analysis/pin_cxb.html

3. Analysis and Results

3.1. Timing Analysis

Fig. 2 shows the XIS light curves in the bands 0.1–1 keV, 1–2 keV, 2–4 keV, 4–7 keV, and 7–11.5 keV, where all the available modules (XIS0, 1, and 3) are combined, and that of the HXD-PIN in the 12–50 keV band. Those of the XIS are after background subtraction with the image region

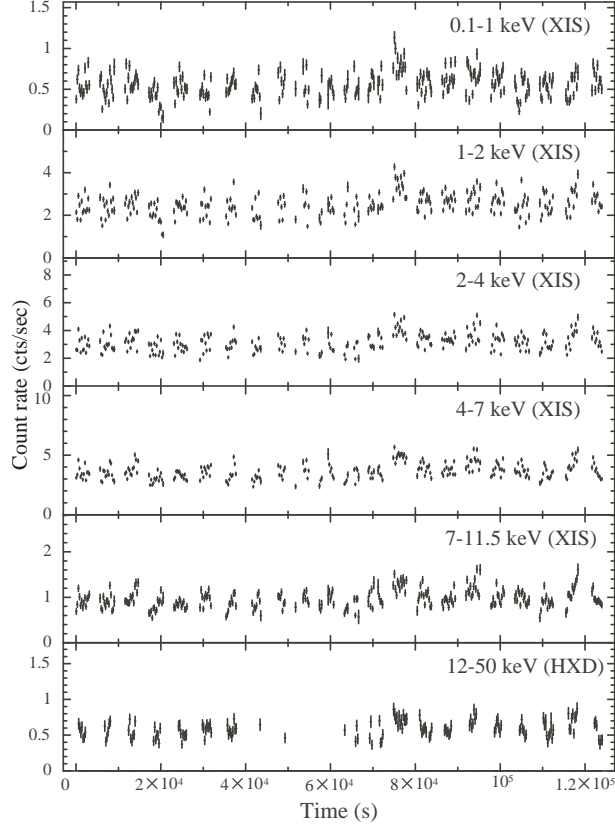


Fig. 2. Energy-resolved light curves of V1223 Sgr subtracted the background with the image region (Fig.1) in the bands 0.1–1 keV, 1–2 keV, 2–4 keV, 4–7 keV, and 7–11.5 keV with the XIS0, 1 and 3 being combined, and only NXB subtracted 12–50 keV from the HXD-PIN. The bin size is 256 sec. The vertical axis of each panel is scaled so that the maximum value is three times as large as the average counting rate. The origin of the time is MJD 54203.50068.

shown in Fig. 1, whereas only the NXB is subtracted in the HXD PIN light curve. Significant signals were detected in all the energy bands. There is an intensity variation associated with the WD rotation ($= 746$ s) as well as a long term one with a time scale of $\sim 10^4$ s. In order to evaluate the period of the WD spin, we first carried out an FFT analysis with the barycentric corrected light curve of the XIS, and identified a rough spin period. We then performed an epoch-folding analysis and produced a periodogram, which is shown in Fig. 3. As a results, we got the period of 745.7 ± 1.1 sec, which is consistent with 745.6 sec (Jablonski & Steiner 1987) measured with an optical photometry. Fig. 4 shows light curves folded at the spin period thus determined. The energy bands are common with those adopted in Fig. 2. The profile of the folded right curves are almost sinusoidal in the energy

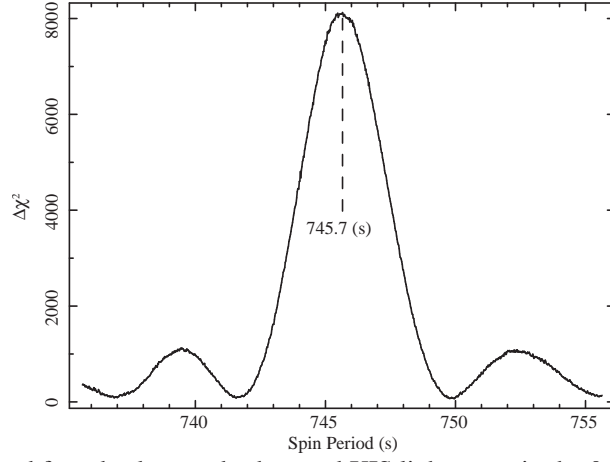


Fig. 3. Periodogram calculated from background subtracted XIS light curve in the 0.5-11.5 keV energy band. The horizontal and vertical axes show trial periods and χ^2 , respectively. The χ^2 values are evaluated with light curves with 31 bin/cycle. The trial period step is 0.01 s. The maximum χ^2 is obtained at the period 745.7 s.

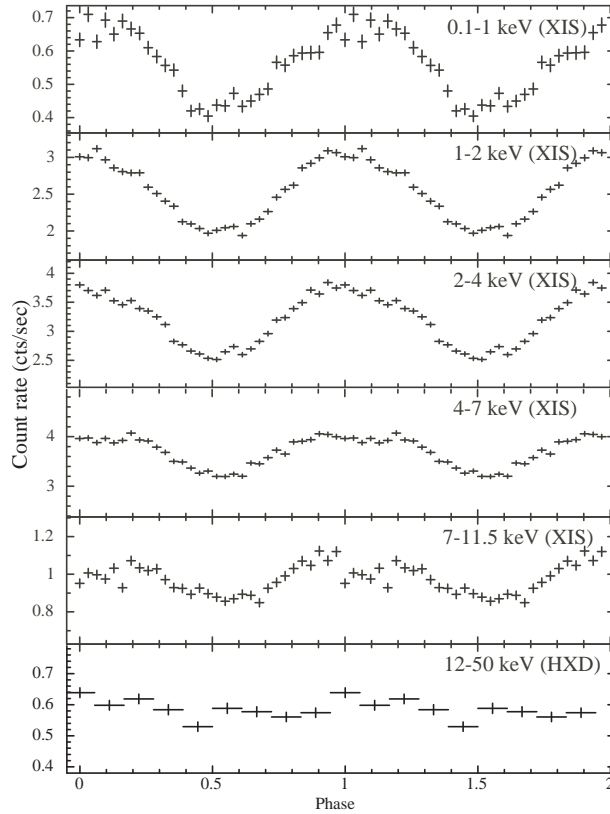


Fig. 4. Folded light curves at the period of 745.7 s. They consist of 31 bins and 9 bins per cycle for the XIS and the HXD-PIN, respectively. The vertical axis of each panel is scaled so that the minimum and the maximum values are 0.65-times and 1.35-times of the averaged counting rate, respectively.

band below 4 keV. In the energy band above 4 keV, on the other hand, a flat profile appear at around the peak phase of the modulation. As shown in Fig. 5, the modulation depth evaluated by fitting the light curves with constant plus sinusoid decreases with increasing energy, which is consistent with

the previous results (Osborne et al. 1985; Taylor et al. 1996).

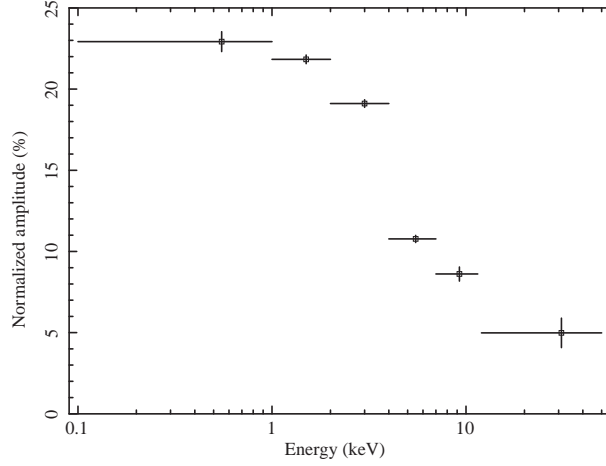


Fig. 5. Fractional spin-modulation amplitude as a function of the X-ray energy.

3.2. Average Spectrum

Fig. 6 shows the averaged spectra of V1223 Sgr after background subtraction according to § 2.2. The spectra from the two FI-CCD modules (XIS0 and XIS3) are co-added. The source is

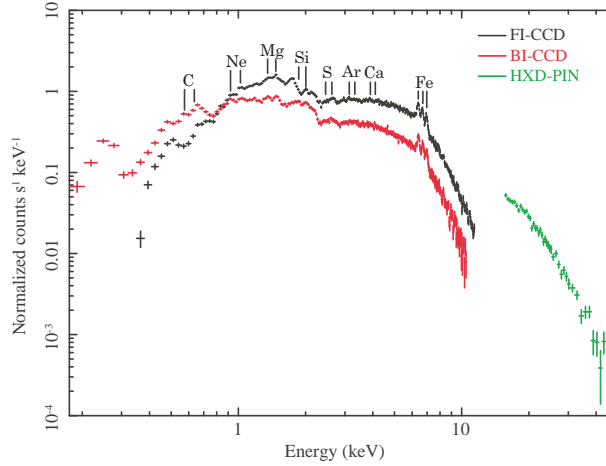


Fig. 6. The averaged spectra of V1223 Sgr. The spectrum of the BI-CCD (XIS1), the FI-CCDs (XIS0 + XIS3) and the HXD-PIN are shown in red, black, and green, respectively.

detected up to 50 keV by the grace of the high sensitivity of the HXD-PIN. In addition to many emission lines from highly ionized metals in the post-shock plasma, a fluorescent iron $K\alpha$ line at 6.4 keV is also prominent, which indicates existence of reflecting cold matter, such as the WD surface and the pre-shock accretion matter.

In order to constrain physical quantities, we have constructed the following model, and fit it to the averaged spectra. We adopted the optically thin thermal plasma emission model `cevmk1` (Done & Osborne 1997) in XSPEC derived from the `mekal` model (Mewe et al. 1985; Mewe et al. 1986; Liedahl et al. 1995; Kaastra et al. 1996) to represent the temperature distribution in the post-

shock plasma (§ 1). The `cevmk1` model introduces the power-law type differential emission measure as

$$d(EM) \propto \left(\frac{T}{T_{\max}}\right)^{\alpha} d(\log T) \propto \left(\frac{T}{T_{\max}}\right)^{\alpha-1} dT, \quad (3)$$

where T_{\max} is the maximum temperature of the plasma. Abundances of the major metals can be set separately in the model. On the assumption that the post-shock accretion column is isobaric (Frank et al. 1992), α becomes equal to 0.5 (Ishida et al. 1994). On the other hand, full theoretical analysis, which takes the pressure gradient and the gravity effect fully into account, predicts $\alpha = 0.43$ (Suleimanov et al. 2005; Falanga et al. 2005).

Since we detected the fluorescent iron $K\alpha$ line at 6.4 keV, we need to take into account a reflected continuum of the plasma emission. To represent the reflection continuum, we adopted the model `reflect` (Magdziarz & Zdziarski 1995) in XSPEC which is a convolution-type model describing the reflectivity of a neutral material. The `reflect` model considers a situation in which a point-like emission source illuminates a thick slab with a solid angle of Ω , and an observer views the slab with an inclination angle of i . We can set the iron abundance and that of the other elements separately. In the spectral fit, we fixed i to the orbital inclination angle 24° (Beuermann et al. 2004) as an average over the WD spin phases. Since the `reflect` model does not include a fluorescent iron line due to its convolution-type nature, we added a Gaussian emission line at 6.4 keV.

In IPs, the spectra undergo strong photoelectric absorption (Norton & Watson 1989; Ezuka & Ishida 1999) which can not be characterized by a single column density. The modeling of the absorption affects the characterization of the intrinsic spectral shape. It is, however, shown that we can avoid this difficulty by using only a moderately high energy band (Ezuka & Ishida 1999) where the multi-column density can be approximated by a single column density. In the analysis hereafter, we use the energy band >5 keV for the XIS. We adopted the `phabs` model in XSPEC in representing the single photoelectric absorption column density.

In the model, we refer to Anders & Grevesse (1989) as the solar abundances of the metals. The abundances of iron and nickel of the `cevmk1` model and that of iron of the `reflect` model are constrained to be the same. In addition, the abundance except for iron of the `reflect` model is synchronized to that of oxygen of the `cevmk1` model, because the surface of the WD is probably covered with the accreted matter and oxygen modifies the reflected continuum, next to iron. Since the other elements do not affect the reflected continuum so severely, their abundances are set equal the solar abundances.

The best-fit model overlaid on the spectra is shown in Fig. 7, and its parameters are summarized in table 2. All the errors are at 90% confidence level. The reduced χ^2 of 1.12 with 313 degree of freedom indicates that the fit is marginally acceptable. The maximum temperature and the power-law index of emission measure of the plasma is obtained to be $T_{\max} = 33.5_{-6.1}^{+7.1}$ keV and $\alpha = 0.58_{-0.17}^{+0.19}$, respectively. Our T_{\max} is consistent with that of Beardmore et al. (2000), 43_{-12}^{+13} keV using the Ginga data in which they adopted the same model scheme to ours (see § 4.1 for more detail). The best-fit α

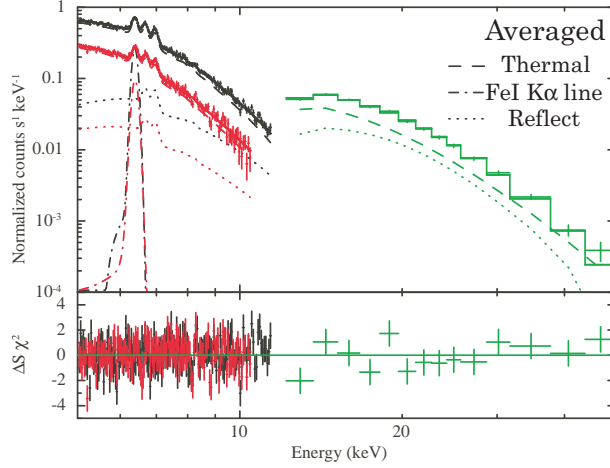


Fig. 7. The best-fit $phabs \times (reflect \times cevmkl + Gaussian)$ model overlaid on the averaged spectra. Black, red and green colors are the same as in Fig. 6. Crosses, solid lines, dashed lines, dotted lines, and dotted-dashed lines represent the data points, the total model, the intrinsic thermal emission model (*cevmkl*), its reflection (*reflect*) model, and the fluorescent iron $K\alpha$ line (*Gaussian*). The lower panel shows the fit residual in a unit of σ .

is consistent both with the value 0.5 predicted by the isobaric post-shock plasma model (Ishida et al. 1994) and with 0.43 based on the full theoretical model (Falanga et al. 2005). The measured solid angle, $\Omega/2\pi = 0.95^{+0.40}_{-0.27}$ can be interpreted as unity, which suggests that the reflector is the WD surface and the shock height is negligibly small compared with the WD radius. It should be noted that the central energy of the iron $K\alpha$ line is slightly smaller than its laboratory value 6.40 keV, and the profile is significantly broad in energy. The oxygen and iron abundances are measured at $Z_O = 1.07^{+0.71}_{-0.39}$ and $Z_{Fe} = 0.29 \pm 0.03$, respectively.

Since our α -free fit results in $\alpha = 0.58^{+0.19}_{-0.17}$ which is consistent with the theoretical value, we fitted to the averaged spectra with the model fixing $\alpha = 0.43$. In this case, the reduced χ -squared value is $\chi^2_\nu = 1.12$ with 314 degree of freedom, similar to that of the α -free fit. T_{\max} calculated at larger value than that of the α -free fit by 4.5 keV, $37.9^{+5.1}_{-4.6}$ keV. $\Omega/(2\pi)$ and Z_O are calculated at slightly smaller values, 0.91 ± 0.26 and $0.86^{+0.40}_{-0.26}$, respectively, the other parameters almost common with the α -free fit. All parameters are consistent with the α -free case within their errors.

3.3. Phase-resolved Spectra

We carried out phase-resolved spectral analysis by sorting the data according to the WD spin phase. First, we created spectra of the phases 0–0.1, 0.1–0.2, 0.2–0.3, ..., 0.9–1.0 in Fig. 4 and calculated the ratios of these spectra to the phase-averaged spectrum. The results are shown in Fig. 8. Significant variation of the spectra is detected below 10 keV where the photoelectric absorption can affects the spectra. By contrast, no significant variation was detected above 10 keV. These results are as expected from the energy dependence of the folded light curves in Fig. 4.

Second, we fitted the model defined in § 3.2 to the spectra and evaluated physical parameters quantitatively in each phase. Considering data statistics, we divided the spectra into the following 8

Table 2. Best-fit parameters of a simultaneous fit to Suzaku averaged spectrum. The adopted model is *phabs*×*reflect*×(*cevmkl*+ *Gaussian*).*

Parameter	Value	
$N_{\text{H}} (\times 10^{22} \text{ cm}^{-2})$	$8.9^{+1.8}_{-1.7}$	$9.1^{+1.7}_{-1.6}$
$T_{\text{max}}^{\dagger} (\text{keV})$	$33.5^{+7.1}_{-6.1}$	$37.9^{+5.1}_{-4.6}$
α^{\ddagger}	$0.58^{+0.19}_{-0.17}$	0.43 (fixed)
$\Omega/(2\pi)^{\S}$	$0.95^{+0.40}_{-0.27}$	0.91 ± 0.26
$i^{\parallel} (\text{deg})$	24 (fixed)	24 (fixed)
$Z_{\text{O}}^{\#}$	$1.07^{+0.71}_{-0.39}$	$0.86^{+0.40}_{-0.26}$
$Z_{\text{Fe}}^{\#}$	0.29 ± 0.03	$0.28^{+0.03}_{-0.02}$
FeI-K α line Energy (keV)	$6.391^{+0.006}_{-0.005}$	$6.391^{+0.006}_{-0.004}$
FeI-K α line sigma (eV)	35^{+13}_{-16}	33^{+10}_{-16}
FeI-K α line <i>EW</i> (eV)	99^{+16}_{-11}	97^{+13}_{-12}
χ^2 (d.o.f.)	350.78 (313)	351.90 (314)

All the uncertainties are at the 90% confidence level.

[†]Maximum temperature of the optically thin thermal plasma.

[‡]Power of DEM as $d(EM) \propto (T/T_{\text{max}})^{\alpha-1} dT$.

[§]Solid angle of the reflector viewed from the plasma.

^{||}Angle between the reflection surface normal and the observer's line of sight.

[#]Based on the solar abundances defined in Anders & Grevesse (1989).

phases: 0–0.25, 0.125–0.375, 0.25–0.5, 0.375–0.625, 0.5–0.75, 0.625–0.875, 0.75–1.0, 0.875–1.125 of Fig. 4. Note that these phases have some mutual overlap. In the fitting, we fixed α at 0.43 (Falanga et al. 2005), which is obtained based on the full theoretical calculation (Suleimanov et al. 2005). We also froze $\Omega/2\pi$ equal to unity, which is consistent with the value from the fit with $\alpha = 0.43$ (table 2). We fixed T_{max} , Z_{O} , and Z_{Fe} at the values obtained from the phase averaged spectral fitting where α was fixed at 0.43 (table 2). On the other hand, the inclination angle of the reflector i was set free to vary because it should depend on the spin of the WD. The 5–50 keV band was used as the averaged spectral analysis.

In Fig. 9, we showed the result of the fit in the 0.875–1.125 phase as an example which covers the peak of the X-ray modulation. The best-fit parameters are summarized in table 3 and are shown in Fig. 10. The fits are generally acceptable at the 90% confidence level. The parameter that shows the most significant spin modulation is hydrogen column density N_{H} , as demonstrated in panel (b), which varies by up to a factor of two among the phases and is inversely correlated with the X-ray light curve. The modulation of i is not clear. Although i seems larger at around the intensity-minimum phase, the statistical errors are somewhat too large as shown in panel (e). The central energy of the fluorescent iron K α line shown in panel (c) shifts significantly from 6.40 keV to maximally 6.38 keV at the intensity-minimum phase, while its width does not change within statistics errors (panel (d)). The

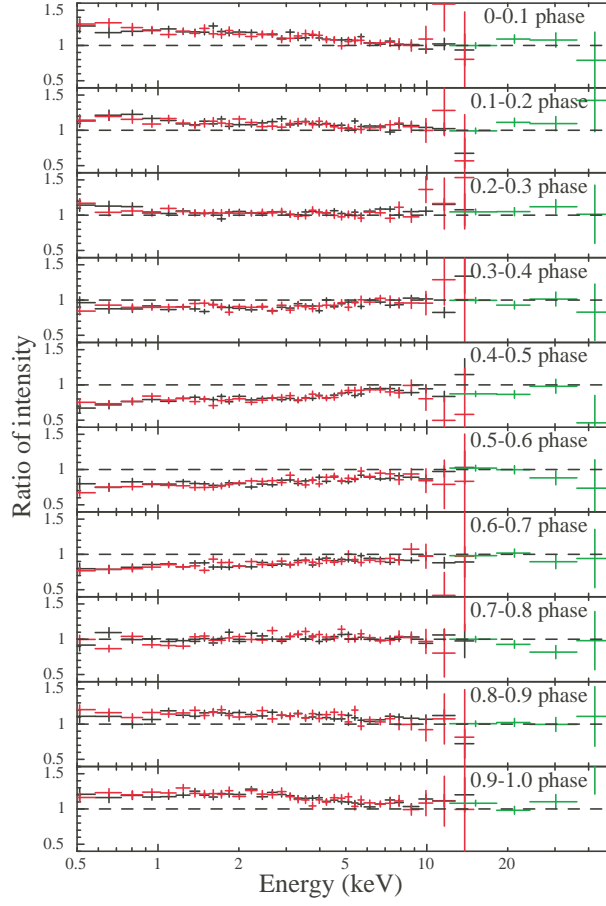


Fig. 8. Ratios of phase-resolved spectra to the averaged spectra. The spin cycle is segmented into 0.1 phase intervals, where the phase 0 corresponds to the rotational intensity-maximum phase. Black, red and green colors are the same as in Fig. 6 and 7.

EW (panel (f)) may be anti-correlated with the X-ray modulation, though it is critical statistically.

At the end of this subsection, we would like to remark on the central energy shift of the 6.4 keV line at the intensity-minimum phase in Fig. 3(c). It is wellknown that the line central energy is sensitive to the evaluation of the slope of underlying continuum. Accordingly, we have simulated the phase-resolved spectra with the `fakeit` command in XSPEC by varying N_{H} in the range $1-50 \times 10^{22} \text{ cm}^{-2}$. In doing this, we used XIS0, 1, 3 and PIN and created combined spectra in the 5-50 keV band with exposure times equal to those of the phase-resolved spectra. The parameters except N_{H} are fixed at the best-fit values (table3). As a result of the fits, we found that the shift of the line central energy is 5 eV at the phase 0.375-0.625 where the central energy shift of 6.4 keV line is maximum. We therefore conclude that the line central energy shift of ~ 20 eV at the rotational intensity minimum phase is real.

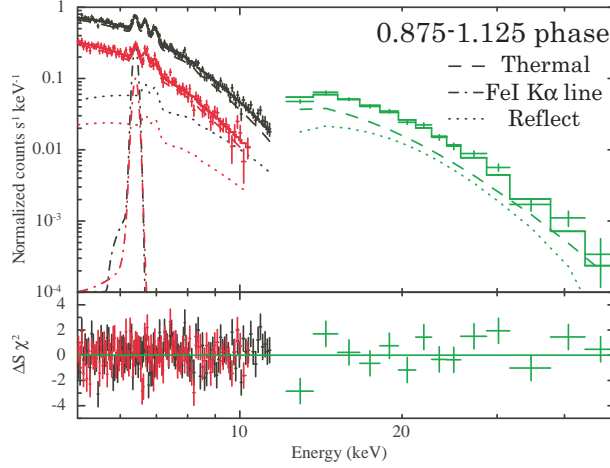


Fig. 9. Best-fit model to the spectra integrated over the 0.875-1.125 phase of Fig. 4. The color assignment is the same as in Fig. 6 through 8.

4. Discussion

4.1. Estimation of mass of WD and comparison with the other observations

As explained in § 1, the temperature at the shock front T_{\max} is represented with Eq. (1). The plasma encountered the shock cools via optically thin thermal plasma emission and finally settles onto the WD. Note that the cyclotron radiation important in polars, which harbor a WD with a magnetic field of as strong as $B \simeq 10^{7-9}$ G (Woelk & Beuermann 1996), can be ignored in V1223 Sgr. With the aid of the WD mass and radius relation by Nauenberg (1972),

$$R_{\text{WD}} = 0.78 \times 10^9 \left[\left(\frac{1.44 M_{\odot}}{M_{\text{WD}}} \right)^{2/3} - \left(\frac{M_{\text{WD}}}{1.44 M_{\odot}} \right)^{2/3} \right]^{1/2} \text{ cm} \quad (4)$$

and the observed T_{\max} calculated with fully theoretical $\alpha = 0.43$ in Eq. (1), we obtained the WD mass and the radius to be $M_{\text{WD}} = 0.82^{+0.05}_{-0.06} M_{\odot}$ and $R_{\text{WD}} = (6.9 \pm 0.4) \times 10^8 \text{ cm}$, respectively.

A number of publications have been made so far on the mass determination of the WD in V1223 Sgr. The results of them are summarized in table 4. As evident from this table, they show a large scatter, amounting to $\sim 0.4 M_{\odot}$. Of them, Suleimanov et al. (2005), Evans & Hellier (2007), Brunschweiler et al. (2009) used data of RXTE, XMM-Newton, and Swift, respectively, and evaluated the mass by taking into account the multi-temperature nature of the post-shock plasma. They, however, do not include the reflection component in their spectral evaluation. Its intensity relative to the direct component, however, increases with increasing X-ray energy due to predominance of the Compton scattering (= Thomson scattering) over the photoelectric absorption. In still higher energies, on the contrary, the reflection component becomes relatively weaker because of reduction of the Compton cross section with increasing X-ray energy. The boundary between these two phenomena appears at $\sim 25 \text{ keV}$, as demonstrated in Fig. 7 and 9. Since the energy band of RXTE and XMM-Newton is effectively limited below $\sim 30 \text{ keV}$, the omission of the reflection component

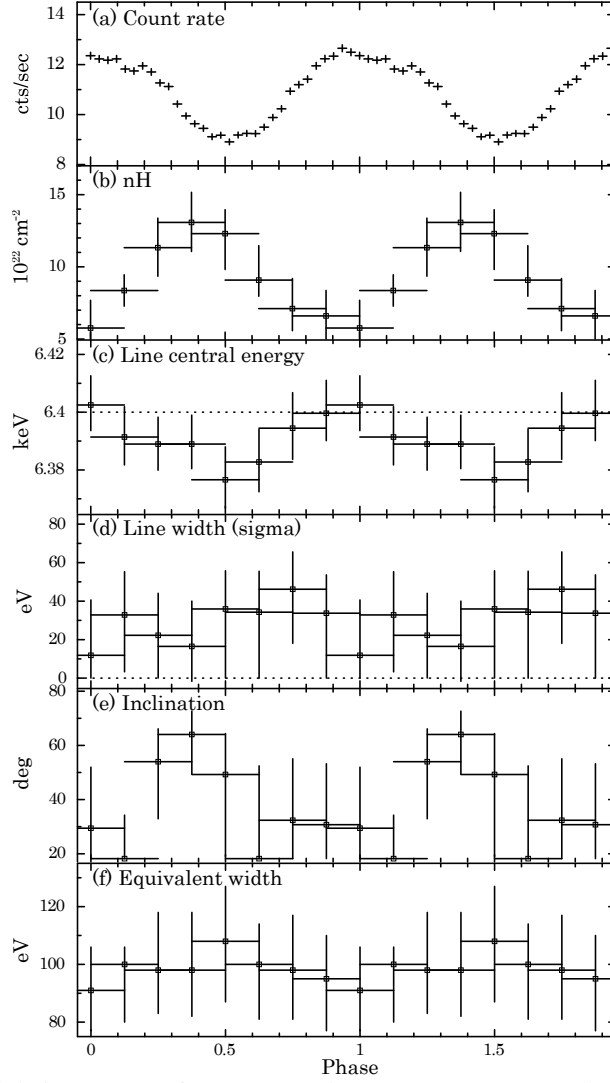


Fig. 10. The rotational modulation curves of (a) 0.1-11.5 keV X-ray count rate, (b) the hydrogen column density N_H , (c) the central energy of the fluorescent $K\alpha$ line, (d) the energy width of the Fe-I $K\alpha$ line, (e) the inclination of the reflector i , and (f) the equivalent width EW of the Fe-I $K\alpha$ line. Modulations of N_H and the center energy of the Fe-I $K\alpha$ line is significant.

leads Suleimanov et al. (2005) and Evans & Hellier (2007) to a T_{\max} evaluation larger than reality. In fact, we fitted our spectra without the reflection component in the 5–30 keV band, and found $kT_{\max} > 100$ keV. Brunschweiler et al. (2009), on the other hand, evaluated kT_{\max} with the Swift data in the 15–100 keV energy band where the reflection component softens spectra. Accordingly, their kT_{\max} is lower than as it is, resulting in a smaller estimation of the WD mass. Since the statistics of our HXD-PIN spectrum is only moderate, we have simulated the HXD-PIN spectrum with the *fakeit* command in XSPEC using the best-fit parameters (§ 3.2), and evaluated it with the model but without the reflection component in the band 15–60 keV. The maximum temperature results in as low as 16 keV.

Revnivtsev et al. (2004) took account of the reflection component, as well as the multi-

temperature nature of the post-shock plasma. Their estimation of the reflector's solid angle, $\Omega/2\pi = 0.35 \pm 0.15$, was smaller than ours by a factor of a few. Beuermann et al. (2004) used the plasma temperature of $kT_{\text{max}} = 43_{-12}^{+13}$ keV estimated by Beardmore et al. (2000) from Ginga. Beardmore et al. (2000) took the multi-temperature nature of the plasma into consideration and the reflection which assumed that the reflector occupy the solid angle of $\Omega/2\pi = 1$, which coincides with our result. Accordingly, their mass range overlaps with ours within statistical error.

Yuasa et al. (2010) adopted a partial covering absorption model, characterized with a covering fraction of $C_{\text{PC}} = 0.5_{-0.02}^{+0.04}$ and a very large hydrogen column density of $n_{\text{H}} = 219_{-25.7}^{+29.7} \times 10^{22} \text{cm}^{-2}$, instead of the reflection component. Cropper et al. (1998) revealed that a partial covering model can mimic the reflection model reasonably well, and the WD mass only slightly change from an estimation based on the reflection model. In fact, their estimation of WD mass of $0.75 \pm 0.05 M_{\odot}$ matches with ours.

It is therefore important to remember that the contribution of the reflection component must be taking into account correctly for evaluating the mass of the WD. Usage of the HXD-PIN onboard Suzaku is one of the best ways to do so in that it has the highest sensitivity at the turnover energy ~ 25 keV among all the instruments so far in orbit.

4.2. *The Nature of the Fluorescent Iron $K\alpha$ Line*

4.2.1. *Origin of the Energy Shift of the Line*

As demonstrated in Fig. 10 and table 3, we detected spin-modulation of the central energy of the fluorescent iron $K\alpha$ line that becomes minimum at the spin-minimum phase. This characteristic can be understood in the framework of the accretion curtain model (Rosen et al. 1988) accepted widely today, in which the X-ray intensity modulation is caused mainly by photoelectric absorption in the pre-shock accretion column. The spin-minimum phase occurs when the upper accretion column points to the observer, at which configuration the observer looks down the post-shock plasma through the pre-shock absorbing matter. At the peak phase, on the other hand, the absorption effect is minimum, and the second pole may appear depending on the inclination angle. The observed line-of-sight hydrogen column density (panel (a) and (b) of Fig. 10) behaves according to this picture. The observed red-shifted fluorescent iron line component can be attributed to the pre-shock accreting matter which flows away from the observer to the WD. Ezuka & Ishida (1999) pointed out based on ASCA observations of ~ 20 mCVs that the fluorescent iron line mainly originates from the WD surface, and indicated significant contribution from the pre-shock accretion column as well if the thickness of the accretion column is $\gtrsim 10^{23} \text{cm}^{-2}$. Since the rotational speed of the WD surface ($= 2\pi R_{\text{WD}}/P_{\text{spin}}$) is 60 km s^{-1} , the energy shift of the line associated with the WD rotation amounts only to ~ 1 eV. Consequently, the energy shift of the iron line is most likely attributed to the contribution from the pre-shock accretion column.

4.2.2. Identification of the Fluorescent Iron $K\alpha$ Line from the Pre-shock Accretion Column

To further confirm the fluorescence Fe line emission originating from the pre-shock accretion column, we looked into the phase-resolved spectra in the 5–8.5 keV band in more detail. First, we fitted the same model as in § 3.3 but with the iron line central energy and its width being fixed at 6.4 keV and 0 keV, respectively. We fixed all the continuum parameters at their best-fit values (table 3), but only the normalization is set free to vary. The top and middle panels of Fig. 11 are the results of the fits to the spectra at the spin-maximum and the spin-minimum phases (0.875–1.125 and 0.375–0.625, respectively, see Fig. 4) of the X-ray intensity modulation. In the spin-maximum phase, it is clear that the structure of the line can be reproduced well only with a single narrow Gaussian. In the spin-minimum phase, on the other hand, a slight wiggle remains centered at ~ 6.25 keV in the residual panel, although the fit itself is statistically acceptable (χ^2 (d.o.f.) = 231.15 (230)).

In order to fill the residual, we added another Gaussian in the model and fitted it to the phase-resolved spectra. The best-fit parameters are summarized in table 5. Here the width of the second Gaussian is fixed at 0 keV. As suggested from Fig. 11, the second Gaussian is found not required at some phases statistically, and hence, we added it only to the phases where significance of the F -test exceeds 80, whose values are listed at the bottom line of table 5. As evident from the table, introduction of the second Gaussian significantly improves the fits at phases close to the spin-minimum phases. The shift of the central energy of the second Gaussian is the largest at the phase 0.25–0.5 where the central energy becomes 6.29 keV. The EW of the component is approximately 30 eV while the uncertainties are somewhat large. The bottom panel of Fig. 11 shows the XIS spectra fitted with the model including the two Gaussians, as an example. The wiggle in the residual plot of the top panel disappears.

4.2.3. Origin of the Red-shifted Iron $K\alpha$ Line

At the spin-minimum phase, we have succeeded in resolving the red-shifted fluorescent iron $K\alpha$ line whose central energy is $6.30^{+0.07}_{-0.05}$ keV at the phase 0.375–0.625. The corresponding line-of-sight velocity is $4.7^{+2.3}_{-3.3} \times 10^3$ km s $^{-1}$. This agrees well with the free-fall velocity onto the WD $= \sqrt{2GM_{\text{WD}}/R_{\text{WD}}} = 5.6 \pm 0.4 \times 10^3$ km s $^{-1}$. Since the pre-shock matter is expected to flow toward the WD at the free-fall speed, and to be maximally red-shifted at the spin-minimum phase, the red-shifted iron line must originate from the pre-shock accreting matter via fluorescence due to irradiation from the post-shock plasma. The WD surface velocity can not explain the observed velocity shift (§ 4.2.1). In the WD rotation picture, relative phasing of the line energy shift with respect to the X-ray intensity modulation is somewhat different from what is observed, and at some phases a blue-shifted component must have been detected.

4.2.4. Verification with equivalent width

The EW of the red-shifted iron line has been estimated to be $EW = 28^{+44}_{-13}$ eV at the 0.375–0.625 phase. The EW of fluorescent iron $K\alpha$ line from point-like source surrounded by matter with a column density of N_{H} by a 2π solid angle

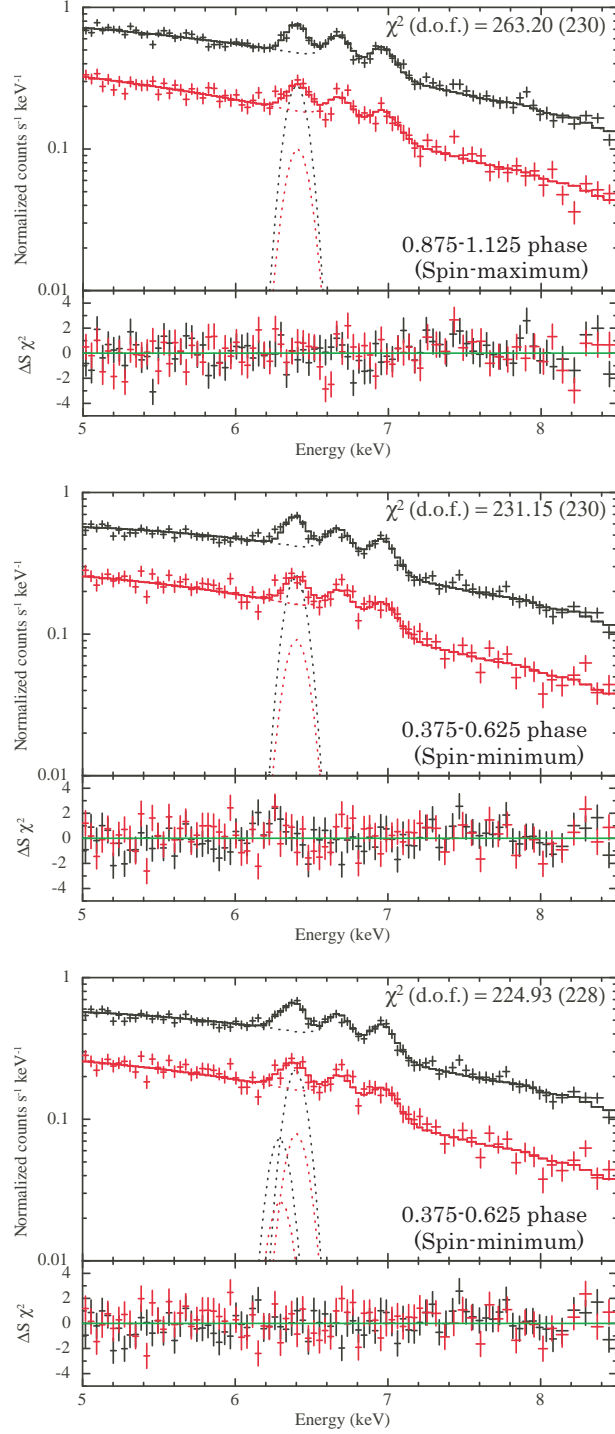


Fig. 11. The 5-8.5 keV spectra fitted with a single Gaussian at the intensity-peak phase 0.875-1.125 (top) and the intensity-minimum phase 0.357-0.625 (middle). The width of the Gaussian is fixed at $\sigma = 0$ keV. (Bottom) The same as the middle panel but fitted with two Gaussians.

$$EW = \frac{1}{2} \beta \frac{N_H}{10^{21} \text{ cm}^{-2}} \quad [\text{eV}] \quad (5)$$

(Ezuka & Ishida 1999). The factor 1/2 is introduced because we consider fluorescence of the accreting matter and hence the hemisphere not occupied by the WD. β is the correction factor of spectral shape

of an ionizing continuum, and $\beta = 1$ if the continuum is a power law with a photon index of 1.1 (Inoue 1985). The EW scales with power of continuum to ionize iron K-shell, and can be described with the ionizing spectrum f_I as

$$EW \propto \frac{1}{f_I(E_{K\alpha})} \int_{E_{K \text{ edge}}}^{\infty} f_I(E) \sigma_{Fe}(E_{K \text{ edge}}, E) dE, \quad (6)$$

where $E_{K \text{ edge}}$ and $E_{K\alpha}$ are the energies of the iron K edge and the central energy of the neutral iron $K\alpha$ line, which are 7.1 keV and 6.4 keV, respectively. $\sigma_{Fe}(E_{K \text{ edge}}, E)$ is the photo ionization cross section of iron K-shell (Band et al. 1990). β can be obtained by the ratio of Eq. (6) calculated with the multi-temperature plasma spectrum to that calculated with a power law with $\Gamma = 1.1$. In our case, the multi-temperature plasma with $kT_{\text{max}} = 37.9$ keV results in $\beta = 0.73$. The hydrogen column density at the spin-minimum phase has been evaluated $N_H = 12.3^{+1.7}_{-2.5} \times 10^{22} \text{ cm}^{-2}$ (table 3). Note that correction of the iron abundance is not necessary in Eq. (5) because both the equivalent width and N_H scale in proportion to the iron abundance. Consequently, the EW of the fluorescent iron $K\alpha$ line from the pre-shock accreting matter is expected to be $EW = 44.9^{+6.2}_{-9.1} \text{ eV}$. This value agrees with the observed one $28^{+44}_{-13} \text{ eV}$.

We note that we have to adopt N_H in Eq.(5) which is averaged over the hemisphere not occupied by the white dwarf. It is, however, impossible to evaluate the averaged N_H because we can measure the thickness of matter on the line of sight. As an approximation, we might have used the phase-average value listed in table 5, since we can observe the post-shock plasma from different directions using the WD rotation. However, line-of-sight N_H varies in a small range $0.58\text{-}1.31 \times 10^{23} \text{ cm}^{-2}$. Accordingly, it does not matter to use the N_H at the spin-minimum phase as a representative, considering the large error on the observed EW .

In summary of this subsection, we detected the iron $K\alpha$ line component whose central energy is modulated synchronized with the WD rotation. Its modulation pattern (maximal energy shift at the X-ray intensity minimum), amount of energy shift, and EW all indicate that the line originates from the pre-shock accreting flow via fluorescence due to irradiation of the post-shock hot plasma emission.

4.3. Height and fractional area of the post-shock accretion column

The intensity of the reflection continuum and the fluorescent iron $K\alpha$ emission line at 6.4 keV from the WD surface are good indicator of the height of the post-shock plasma since they both depend upon the solid angle of the plasma viewed from the WD. In this subsection we intend to constrain the plasma height from these observed quantities, and then try to evaluate the size of the fractional accreted area on the WD surface.

As mentioned in § 3.2, the solid angle of the WD surface is measured to be $\Omega/2\pi = 0.91 \pm 0.26$ through the spectral fitting to the averaged spectra. The result is consistent with $\Omega = 2\pi$, implying that the height of the post-shock plasma is negligibly small compared with the WD radius. The upper limit of the height h_Ω is obtained from the lower limit of Ω , which results in $h_\Omega < 0.07 R_{WD}$, assuming

that the post shock plasma is point-like.

A similar estimation can be carried out using the EW of the 6.4 keV iron line in the framework of George & Fabian (1991), in which they evaluated the 6.4 keV line EW in a geometry composed of a point-like X-ray source locating above an infinite optically thick slab. In their scheme, George & Fabian (1991) assumed that the irradiating spectrum from the point-like source is a power-law with various photon indices. They assumed the iron abundance of the slab to be $[\text{Fe}/\text{H}] = 3.2 \times 10^{-5}$. The X-ray spectrum of V1223 Sgr is, on the other hand, a multi-temperature plasma emission with the maximum temperature of 37.9 keV. Since the temperature is very high, the spectrum can be approximated with a power law at energies which ionize a K-shell electron of iron efficiently ($E \gtrsim E_{\text{K edge}} = 7.1$ keV). To identify the power-law model that represents the observed continuum best, we produced a simulated XIS spectrum based on the multi-temperature plasma emission model which best-fits the phase-averaged spectra (Fig. 7 and table 2) using the `fakeit` command in XSPEC, and fitted it with a power law. As a result, we found the irradiating spectrum can be approximated with a power law with $\Gamma = 1.46$. Our estimation of the iron abundance 0.28 is based on the assumption of $[\text{Fe}/\text{H}] = 4.68 \times 10^{-5}$. In the scheme of George & Fabian (1991), we should use the value $Z_{\text{Fe}} = 0.41$ after correction of the abundance difference in solar abundance.

After all these manipulations, the EW expected from V1223 Sgr in the case of negligible height plasma is obtained to be ~ 80 eV, which is consistent with the observed $EW = 80^{+13}_{-51}$ eV at the spin-minimum 0.375–0.625 phase (table 5). Consequently, the EW of fluorescent iron $\text{K}\alpha$ line is also consistent with a picture in which the height of the plasma is negligibly small. The upper limit of the plasma height $h_{\text{K}\alpha}$ estimated from the lower bound of the observed EW ($= 29$ eV) is $h_{\text{K}\alpha} < 0.15 R_{\text{WD}}$. Adopting the limit on h_{Ω} , we conclude that the height of the post-shock plasma is less than 7 % of the WD radius.

In a one-dimensional accretion flow model dominated by bremsstrahlung cooling Aizu (1973), which can be applied to V1223 Sgr, the height of the plasma can be analytically solved as

$$h_c = 0.605 v_s t_c, \quad (7)$$

where v_s is the velocity of the post-shock plasma at the shock front, which is

$$\begin{aligned} v_s &= \frac{1}{4} \sqrt{\frac{2GM_{\text{WD}}}{R_{\text{WD}}}} \\ &= 1.40 \times 10^8 \text{ [cm s}^{-1}\text{]} \end{aligned} \quad (8)$$

in the case of a strong shock, where we adopt $M_{\text{WD}} = 0.82 M_{\odot}$ and $R_{\text{WD}} = 6.9 \times 10^8$ cm, obtained in this work (§ 4.1). t_c is the cooling time scale at the shock front

$$\begin{aligned} t_c &= 3kT_{\text{max}} / (2\mu m_H \epsilon_{\text{ff}}) \\ &= 4.20 \times 10^{-13} T^{1/2} \rho_s^{-1} \text{ [s]}, \end{aligned} \quad (9)$$

in the c.g.s. unit, where ϵ_{ff} is the bremsstrahlung emissivity with the Gaunt factor of 1.10 from Born approximation, and ρ_s is the density of the post-shock plasma at the shock front, which can be

described as

$$\rho_s = \frac{\dot{M}}{4\pi f R_{\text{WD}}^2 v_s}, \quad (10)$$

Of the quantities in Eq. (10), \dot{M} can be evaluated from the observed bolometric flux $F_{0.1-100} = 4.0 \times 10^{-10} \text{ erg cm}^{-2} \text{ s}^{-1}$ together with $D = 527 \text{ pc}$ (Beuermann et al. 2004), which is

$$\begin{aligned} \dot{M} &= \frac{L_{0.1-100} R_{\text{WD}}}{GM_{\text{WD}}} = \frac{4\pi D^2 F_{0.1-100} R_{\text{WD}}}{GM_{\text{WD}}} \\ &= 8.4 \times 10^{16} \text{ [g s}^{-1}] \end{aligned} \quad (11)$$

Inserting Eqs. (8)–(11) into Eq. (7), we obtained $h_c = 7.4f \times 10^9 \text{ cm}$. From the constraint $h_c = h_\Omega < 0.07 R_{\text{WD}}$, we obtain $f < 0.007$.

Hellier (1997) gave upper limit of $f < 0.002$ in the eclipsing IP XY Arietis which is similar to our result. According to Revnivtsev et al. (2004), $f \simeq 0.01$ based on their estimation of $h_c = 1.1 \times 10^{10} f \text{ cm}$ from bolometric luminosity and $\Omega/2\pi < 0.5$. This result, however, indicates that the height of the accretion column is more than 15% of the WD surface, which seems unrealistically large for a high accretion rate system like V1223 Sgr.

5. Conclusion

We have reported results of the Suzaku observation of the typical IP V1223 Sgr in 2007 April. The 5-50 keV X-ray spectra of V1223 Sgr can be reproduced with a multi-temperature optically thin thermal plasma emission model and its reflection from the WD surface, which suffer photoelectric absorption represented by a single hydrogen column density, and iron $K\alpha$ emission lines from the WD surface and the pre-shock accreting matter as well. The WD spin period is measured to be $745.7 \pm 1.1 \text{ s}$, and the amplitude of the X-ray modulation is deeper in higher energy bands. This modulation is mainly caused by a rotational modulation of the hydrogen column density of order $N_{\text{H}} \simeq 10^{23} \text{ cm}^{-2}$, which is twice as large in the spin-minimum phase as in the spin-maximum phase. This fact is consistent with the accretion curtain model in which the observer looks down the upper accretion pole in the spin-minimum phase.

From the spectral analysis, the power index of the temperature distribution α ($d(EM) \propto T^{\alpha-1} dT$) is found to be $0.58_{-0.17}^{+0.19}$, which agrees with the value of 0.43 (Falanga et al. 2005) derived based on the full theoretical calculation of the one-dimensional post-shock accretion flow (Suleimanov et al. 2005). By freezing $\alpha = 0.43$, we have obtained the maximum temperature of the post-shock plasma to be $kT_{\text{max}} = 37.9_{-4.6}^{+5.1} \text{ keV}$, from which we calculated the mass and the radius of the WD as $M_{\text{WD}} = 0.82_{-0.06}^{+0.05} M_\odot$ and $R_{\text{WD}} = (6.9 \pm 0.4) \times 10^8 \text{ cm}$ with the aid of a WD mass-radius relation. We compared our mass value with the other previous works in detail which show a large mutual inconsistency as large as $0.4 M_\odot$. We demonstrated that it is essentially important to take into account the reflection component appropriately for evaluating the mass of the WD from X-ray spectroscopy.

We have found a spin modulation of the central energy of the fluorescent iron $K\alpha$ emission line for the first time in magnetic-CVs which varies between 6.38 keV and 6.40 keV with the maximum red-shift at the spin-minimum phase. More detailed analysis has revealed that the iron line can be decomposed into a stable 6.4 keV component and another red-shifted component which manifests itself around the spin-minimum phase at an energy of ~ 6.3 keV. The equivalent Doppler velocity of the latter component $4.7^{+2.3}_{-3.3} \times 10^3 \text{ km sec}^{-1}$ and its observed EW of 28^{+44}_{-13} eV are both consistent with an interpretation that it originates from the pre-shock accreting matter via fluorescence due to irradiation of the post-shock hot plasma emission. The observed EW of the former stable component, on the other hand, is ~ 80 eV. Considering the ionizing power of the irradiating thermal spectrum and the observed iron abundance, we have confirmed that the iron $K\alpha$ line with this amount of EW can be emitted from the WD surface via fluorescence. The shock height is evaluated to be small enough compared to the radius of the WD.

The shock height of the plasma can be evaluated also from the intensity of the reflected continuum component. The solid angle of the WD viewed from the post-shock plasma of $\Omega/2\pi = 0.91 \pm 0.26$ indicates that the shock height is negligibly small compared with the WD radius ($\Omega/2\pi = 1$) as in the case of the stable component of the iron 6.4 keV line. The upper limit of the shock height is obtained to be 7 % of the WD radius ($h_{K\alpha} < 0.07 R_{WD}$). Comparing this estimate to the height predicted by a one-dimensional bremsstrahlung-cooling model of the accretion column, the fraction area of the WD onto which the accretion really takes place is limited to be $f < 0.007$, which is the tightest constrain on f among the non-eclipsing IPs. This estimate is comparable to the eclipsing IP XY Ari.

6. Acknowledgement

The authors are grateful to all the Suzaku team members for their efforts in the production and the maintenance of instruments and software, spacecraft operation, and calibrations. We would like to thank referee for his very useful comments.

References

- Aizu, K. 1973, Progress of Theoretical Physics, 50, 344
- Anders, E., & Grevesse, N. 1989, Geochim. Cosmochim. Acta, 53, 197
- Arnaud, K. A. 1996, Astronomical Data Analysis Software and Systems V, 101, 17
- Band, I. M., Trzhaskovskaia, M. B., Verner, D. A., & Iakovlev, D. G. 1990, A&A, 237, 267
- Beardmore, A. P., Osborne, J. P., & Hellier, C. 2000, MNRAS, 315, 307
- Beuermann, K., Harrison, T. E., McArthur, B. E., Benedict, G. F., Gänsicke, B. T. 2004, A&A, 419, 291
- Boldt, E. 1987, Phys. Rep., 146, 215
- Brunschweiler, J., Greiner, J., Ajello, M., & Osborne, J. 2009, A&A, 496, 121
- Cropper, M., Ramsay, G., & Wu, K. 1998, MNRAS, 293, 222
- Done, C., & Osborne, J. P. 1997, MNRAS, 288, 649

- Evans, P. A., & Hellier, C. 2007, *ApJ*, 663, 1277
- Ezuka, H., & Ishida, M. 1999, *ApJS*, 120, 277
- Falanga, M., Bonnet-Bidaud, J. M., & Suleimanov, V. 2005, *A&A*, 444, 561
- Frank, J., King, A., & Raine, D. 1992, *Science*, 258, 1015
- Fukazawa, Y., et al. 2009, *PASJ*, 61, 17
- George, I. M., & Fabian, A. C. 1991, *MNRAS*, 249, 352
- Hellier, C. 1997, *MNRAS*, 291, 71
- Hōshi, R. 1973, *Progress of Theoretical Physics*, 49, 776
- Inoue, H. 1985, *Space Science Reviews*, 40, 317
- Ishida, M., Okada, S., Hayashi, T., Nakamura, R., Terada, Y., Mukai, K., & Hamaguchi, K. 2009, *PASJ*, 61, 77
- Ishida, M., Makishima, K., Mukai, K., & Masai, K. 1994, *MNRAS*, 266, 367
- Jablonski, F., & Steiner, J. E. 1987, *ApJ*, 323, 672
- Kaastra, J. S., Mewe, R., & Nieuwenhuijzen, H. 1996, *UV and X-ray Spectroscopy of Astrophysical and Laboratory Plasmas*, 411
- Kokubun, M., et al. 2007, *PASJ*, 59, 53
- Koyama, K., et al. 2007, *PASJ*, 59, 23
- Liedahl, D. A., Osterheld, A. L., & Goldstein, W. H. 1995, *ApJL*, 438, L115
- Magdziarz, P., & Zdziarski, A. A. 1995, *MNRAS*, 273, 837
- Makishima, K. 1986, in *The Physics of Accretion onto Compact Objects*, ed. K. O. Mason, M. G. Watson, & N. E., White (Berlin:Springer) 249
- Mewe, R., Gronenschild, E. H. B. M., & van den Oord, G. H. J. 1985, *A&AS*, 62, 197
- Mewe, R., Lemen, J. R., & van den Oord, G. H. J. 1986, *A&AS*, 65, 511
- Mitsuda, K., et al. 2007, *PASJ*, 59, 1
- Nakajima, H., et al. 2008, *PASJ*, 60, 1
- Nauenberg, M. 1972, *ApJ*, 175, 417
- Norton, A. J., & Watson, M. G. 1989, *MNRAS*, 237, 853
- Osborne, J. P., Rosen, R., Mason, K. O., & Beuermann, K. 1985, *Space Science Reviews*, 40, 143
- Evans, P. A., & Hellier, C. 2007, *ApJ*, 663, 1277
- Revnivtsev, M., Lutovinov, A., Suleimanov, V., Sunyaev, R., & Zheleznyakov, V. 2004, *A&A*, 426, 253
- Rosen, S. R., Mason, K. O., & Cordova, F. A. 1988, *MNRAS*, 231, 549
- Serlemitsos, P. J., et al. 2007, *PASJ*, 59, 9
- Suleimanov, V., Revnivtsev, M., & Ritter, H. 2005, *A&A*, 435, 191
- Steiner, J. E., Schwartz, D. A., Jablonski, F. J., Busko, I. C., Watson, M. G., Pye, J. P., & McHardy, I. M. 1981, *ApJL*, 249, L21
- Takahashi, T., et al. 2007, *PASJ*, 59, 35
- Terada, Y., et al. 2008, *PASJ*, 60, 25
- Woelk, U., & Beuermann, K. 1996, *A&A*, 306, 232
- Yuasa, T., Nakazawa, K., Makishima, K., Saitou, K., Ishida, M., Ebisawa, K., Mori, H., & Yamada, S. 2010, *A&A*, 520, A25

Table 3: Best-fit parameters of the phase resolved spectra.

Phase	0.875-1.125	0-0.25	0.125-0.375	0.25-0.5	0.375-0.625	0.5-0.75	0.625-0.875	0.75-1
$N_H (\times 10^{22} \text{ cm}^{-2})$	$5.8^{+1.9}_{-1.4}$	8.4 ± 1.1	11.3 ± 2.0	$13.1^{+2.1}_{-2.0}$	$12.3^{+1.7}_{-2.5}$	$9.1^{+2.4}_{-1.1}$	$7.1^{+2.1}_{-1.5}$	6.6 ± 1.8
T_{\max}^* (keV)	37.9 (fixed)	37.9 (fixed)	37.9 (fixed)	37.9 (fixed)	37.9 (fixed)	37.9 (fixed)	37.9 (fixed)	37.9 (fixed)
α^\dagger	0.43 (fixed)	0.43 (fixed)	0.43 (fixed)	0.43 (fixed)	0.43 (fixed)	0.43 (fixed)	0.43 (fixed)	0.43 (fixed)
$\Omega/(2\pi)^\ddagger$	1 (fixed)	1 (fixed)	1 (fixed)	1 (fixed)	1 (fixed)	1 (fixed)	1 (fixed)	1 (fixed)
i^\S	29^{+23}_{-11}	≤ 34	54^{+12}_{-21}	64^{+9}_{-15}	49^{+15}_{-30}	≤ 52	32^{+23}_{-14}	31^{+22}_{-13}
Z_O^\S	0.86 (fixed)	0.86 (fixed)	0.86 (fixed)	0.86 (fixed)	0.86 (fixed)	0.86 (fixed)	0.86 (fixed)	0.86 (fixed)
Z_{Fe}^\S	0.28 (fixed)	0.28 (fixed)	0.28 (fixed)	0.28 (fixed)	0.28 (fixed)	0.28 (fixed)	0.28 (fixed)	0.28 (fixed)
FeI-K α line Energy (keV)	$6.403^{+0.010}_{-0.009}$	$6.391^{+0.011}_{-0.010}$	6.389 ± 0.009	$6.389^{+0.010}_{-0.009}$	$6.377^{+0.011}_{-0.010}$	$6.383^{+0.011}_{-0.010}$	$6.394^{+0.012}_{-0.011}$	$6.400^{+0.011}_{-0.009}$
FeI-K α line sigma (eV)	12^{+29}_{-12}	33^{+22}_{-30}	22^{+22}_{-22}	16^{+24}_{-16}	36^{+20}_{-36}	34^{+21}_{-34}	46^{+19}_{-28}	34^{+20}_{-34}
FeI-K α line EW (eV)	91^{+15}_{-14}	100^{+6}_{-20}	98^{+20}_{-15}	98^{+20}_{-16}	108^{+19}_{-21}	100^{+14}_{-19}	98^{+19}_{-17}	95^{+15}_{-18}
χ^2 (d.o.f.)	262.58 (226)	248.00 (226)	244.01 (226)	241.27 (226)	217.05 (226)	265.77 (226)	205.86 (226)	246.63 (226)

*Maximum temperature of the post-shock plasma.

† Power index of DEM as $dEM \propto (T/T_{\max})^{\alpha-1} dT$.

‡ Solid angle of the reflector subtending over the post-shock plasma.

§ Based on the solar abundances defined in Anders & Grevesse (1989).

Table 4. Collection of WD mass estimation in the V1223 Sgr.

Telescope	Energy band (keV)	$M_{\text{WD}}(M_{\odot})$	Reference
Ginga	2-20	0.93 ± 0.12	Beuermann et al. (2004)
RXTE & INTEGRAL	3-100	0.71 ± 0.03	Revnivtsev et al. (2004)
RXTE	3-80	0.95 ± 0.05	Suleimanov et al. (2005)
XMM-Newton	0.2-10	$1.046^{+0.049}_{-0.012}$	Evans & Hellier (2007)
Swift	15-100	0.65 ± 0.04	Brunschweiler et al. (2009)
Suzaku	4-50	0.75 ± 0.05	Yuasa et al. (2010)
Suzaku	5-50	$0.82^{+0.05}_{-0.06}$	This work

Table 5: Best-fit parameters of the phase resolved spectra with two Gaussians.

Phase	0.875-1.125	0-0.25	0.125-0.375	0.25-0.5	0.375-0.625	0.5-0.75	0.625-0.875	0.75-1
FeI-K α line Energy [†] (keV)	6.4 (fixed)	6.4 (fixed)	6.4 (fixed)	6.4 (fixed)	6.4 (fixed)	6.4 (fixed)	6.4 (fixed)	6.4 (fixed)
FeI-K α line sigma [†] (eV)	0 (fixed)	0 (fixed)	0 (fixed)	0 (fixed)	0 (fixed)	0 (fixed)	0 (fixed)	0 (fixed)
FeI-K α line EW^{\dagger} (eV)	90^{+8}_{-9}	95^{+11}_{-7}	86^{+19}_{-80}	91^{+14}_{-91}	80^{+13}_{-51}	83^{+13}_{-44}	92^{+11}_{-7}	92^{+11}_{-7}
FeI-K α line Energy [‡] (keV)	-	-	$6.33^{+0.07}_{-0.22}$	$6.29^{+0.10}_{-0.11}$	$6.30^{+0.07}_{-0.05}$	$6.31^{+0.05}_{-0.06}$	-	-
FeI-K α line sigma [‡] (eV)	0 (fixed)	0 (fixed)	0 (fixed)	0 (fixed)	0 (fixed)	0 (fixed)	0 (fixed)	0 (fixed)
FeI-K α line EW^{\ddagger} (eV)	-	-	25^{+90}_{-23}	13^{+102}_{-11}	28^{+44}_{-13}	24^{+71}_{-15}	-	-
χ^2 (d.o.f.)	263.20 (230)	210.09 (230)	243.91 (228)	240.27 (228)	224.93 (228)	264.75 (228)	245.60 (230)	247.92 (230)
Significance [§] (%)	-	-	83.5	83.9	95.5	97.5	-	-

[†]The component stable in energy.[‡]The red-shifted component.[§]Significance of F -test for adding a second Gaussian to fluorescent iron K α line